Model-Resolution-Based Basis Pursuit Deconvolution Improves Diffuse Optical Tomographic Imaging

Jaya Prakash, Hamid Dehghani, Brian W. Pogue, and Phaneendra K. Yalavarthy*

***Abstract*—The image reconstruction problem encountered in diffuse optical tomographic imaging is ill-posed in nature, necessitating the usage of regularization to result in stable solutions. This regularization also results in loss of resolution in the reconstructed images. A frame work, that is attributed by model-resolution, to improve the reconstructed image characteristics using the basis pursuit deconvolution method is proposed here. The proposed method performs this deconvolution as an additional step in the image reconstruction scheme. It is shown, both in numerical and experimental gelatin phantom cases, that the proposed method yields better recovery of the target shapes compared to traditional method, without the loss of quantitativeness of the results.**

***Index Terms*—Basis pursuit deconvolution, diffuse optical tomography, image reconstruction, near infrared imaging.**

I. Introduction

SOFT tissue imaging using near infrared light (NIR), having wavelength range of 600–1000 nm, has become a promising physiological imaging modality due to the nonionizing nature of radiation [1]–[3]. Diffuse optical tomography, which uses this NIR light as the probing media, exploits the high intrinsic contrast provided by the soft tissue with main applications being brain and breast imaging [1]–[4]. Estimating the internal distribution of optical properties using NIR light measurements acquired at the boundary is a critical step in diffuse optical tomography [5], [6]. Unlike X-ray imaging, NIR light interaction within the tissue is dominated by scattering rather than absorption [5], resulting in loss of resolution in the reconstructed optical images.

Reconstruction of the optical parameters using the limited boundary measurements, also known as the inverse problem, is an ill-posed and under-determined problem (limited boundary data) leading many possible solutions [7], [8]. Constraining the solution space via regularization is one of the common approaches for solving the inverse problem, resulting in most popular Gauss-Newton image reconstruction scheme. The addition of regularization also results in loss of resolution characteristics of the Tikhonov solution, but often necessary for enabling the computation of optical images [7], [8]. Even though there is inherent limitation on the achievable spatial resolution of optical images due to the dominance of scattering at NIR wavelengths, the reconstructed optical images typically appear to be blobby/blurry in nature with less ability to recover shapes using standard reconstruction techniques. The main source of this blur, other than the diffusion of light, is the regularization used for stabilizing the inverse problem. As one can not perform the image reconstruction without the aid of regularization in these cases, there is a considerable interest in methods that can minimize the effect of regularization and reduce the blur caused by it.

The choice of the regularization scheme that is deployed in performing the diffuse optical image reconstruction depends on the prior information available to the user about the noise characteristics of the data and expected image characteristics [7]–[11]. These regularization schemes can be as advanced as utilizing the structural priors available in dual-modality diffuse optical imaging [7], [8]. More importantly, the simple standard regularization schemes like Tikhonov method, that imposes quadratic penalty, assumes that the expected optical image is piece-wise constant and smooth in nature [5], [7]. Thus, it leads to loss of sharp features in the reconstructed images.

Deblurring of diffuse optical images has shown some promise in recovering the target shapes [12]–[14], these methods had used forward operator characteristics and built an information spread function (ISF) independent of image reconstruction procedure. In the proposed work, the aim is to build the ISF or its equivalent in an integrated approach with inclusion of regularization. The image deblurring/deconvolution approaches work at their best in terms of restoration of blurred images when the ISF contains all sources of blurring. The deconvolution is typically performed by using constrained deconvolution method and least squares filtering method [15],

Manuscript received October 11, 2013; revised December 19, 2013; accepted December 30, 2013. Date of publication January 02, 2014; date of current version March 31, 2014. This work was supported in part by the Royal Academy of Engineering, U.K., through Research Exchange Award. The work of P. K. Yalavarthy was supported by the Government of India through Department of Biotechnology (DBT) Rapid Grant for Young investigator (RGYI) (BT/PR6494/GDB/27/415/2012) and DBT Bioengineering Grant (BT/PR7994/MED/32/284/2013). The work of J. Prakash was supported by the Microsoft Corporation and Microsoft Research India under the Microsoft Research India Ph.D. Fellowship Award and SPIE Optics and Photonics Education Scholarship. *Asterisk indicates corresponding author.*

J. Prakash is with the Supercomputer Education and Research Centre, Indian Institute of Science, Bangalore 560 012, India (e-mail: pnjayaprakash88@gmail.com).

H. Dehghani is with the School of Computer Science, University of Birmingham, B15 2TT Birmingham, U.K. (e-mail: h.dehghani@cs.bham.ac.uk).

B. W. Pogue is with the Thayer School of Engineering, Dartmouth College, Hanover, NH 03755 USA (e-mail: brian.w.pogue@dartmouth.edu).

*P. K. Yalavarthy is with the Supercomputer Education and Research Centre, Indian Institute of Science, Bangalore 560 012, India (e-mail: phani@serc.iisc.in).

Digital Object Identifier 10.1109/TMI.2013.2297691

[16]. The reconstructed optical images can also be improved by usage of shape-recovery algorithms [17]–[20], all of them require shape-based parameterization, which are computationally expensive algorithms compared to the traditional Gauss-Newton image reconstruction method. These edge-preserving regularization methods deploy a first-order difference matrix [19], [20], which tend to be computationally expensive step for large problems. The method proposed in this work does not have this requirement. The most computationally expensive step in the proposed method involves singular value decomposition (SVD), which is commonly used in performing diffuse optical tomographic reconstruction [1], [21]. Also, the proposed method is aimed at removing the blur introduced by usage of regularization, making this universally appealing irrespective of the regularization scheme deployed.

In the recent past, there is considerable interest in the image deconvolution using basis pursuit deconvolution, resulting in set of compressive sensing techniques based on ℓ_1-norm minimization forming the state of the art image restoration methods [22]–[26]. Basis pursuit deconvolution/denoising (BPDN)-type methods have been used previously in diffuse optical tomographic image reconstruction as an alternative to traditional Gauss-Newton image reconstruction, having advantage of providing better contrast recovery and improving the spatial resolution of the reconstructed images [27]–[32]. This work aims at deploying the BPDN method coupled with model-resolution matrix [33] to deconvolve the reconstructed optical images using Gauss-Newton minimization scheme. The model-resolution matrix is built using the Jacobian and regularization (representing the model) making it the required blur matrix (convolution matrix) [33]. In the previous work [34], the model-resolution characteristics were incorporated into the reconstruction procedure via regularization matrix. In this work, the model-resolution matrix is built and used as the blurring model in performing the deconvolution of images obtained using a standard reconstruction method.

The basis pursuit deconvolution is achieved through usage of *spilt augmented Lagrangian shrinkage algorithm* (SALSA), which is a well-established method [35], [36]. In this work, a SVD was adapted both for image reconstruction and deconvolution as it provides highly computational efficient framework. It is proven using both numerical and experimental gelatin phantom results that the basis pursuit deconvolution improves both quantitation and quality of the reconstructed optical images. Moreover, the shape recovery of target is much improved using the proposed method. As the emphasis is on presenting a novel approach in improving diffuse optical tomographic image reconstruction using basis pursuit deconvolution, the discussion is limited to continuous wave (CW) 2-D case, where only optical absorption coefficient becomes the unknown.

II. Continuous Wave Diffuse Optical Tomography

A. Forward Model

CW NIR light propagation in diffuse optical tomography is modeled as a steady-state diffuse equation (DE) [37]–[39] which is given as

$$-\nabla \cdot [\kappa(r)\nabla\Phi(r)] + \mu_a(r)\Phi(r) = q_o(r) \tag{1}$$

where $\Phi(r)$ and $q_o(r)$ represents the photon density (real values) and the isotropic CW light source at position r, respectively. The optical diffusion coefficient is represented by $\kappa(r)$, by definition

$$\kappa(r) = \frac{1}{3[\mu_a(r) + \mu_s'(r)]} \tag{2}$$

with $\mu_a(r)$ and $\mu_s'(r)$ representing the optical absorption and optical scattering coefficients. For the CW-case, it is assumed that $\mu_s'(r)$ is known and uniform through out the imaging domain. The partial differential equation in (1) is solved for calculating Φ using a well-established finite element method [37]–[39]. Modeled data $(G(\mu_a))$ is found by sampling the photon density $(\Phi(r))$ at measurements position, i.e., $G(\mu_a) = S\{\Phi\}$, where S is representing the sampling matrix (containing source/detector positions). Using the Rytov approximation experimental data y becomes the natural logarithm of intensity $(\ln(A))$ for a given distribution of μ_a [40], where A represents the amplitude. Robin (Type-III) boundary condition is used to account for refractive index mismatch at the boundaries [40].

B. Standard Method (Inverse Model)

The inverse problem is performed by matching the modeled data (obtained from the forward model) with the experimental data in a least-square sense [1], [5]–[7], [38]. A regularization term is added for stabilizing the inverse problem leading to a objective function

$$\Omega = \|y - G(\mu_a)\|^2 + \lambda\|\mu_a - \mu_{a0}\|^2 \tag{3}$$

where λ is the regularization parameter which is used to constrain the solution space and obtain a stable solution [7]. It is kept constant through out the image reconstruction procedure. The initial guess is represented as μ_{a0}, which is obtained by calibration procedures as explained in [41]. Using the first-order condition of (3) and linearizing the Taylor series expansion of the nonlinear inverse problem results in an update equation of the form [7]

$$\triangle\mu_a = [J^T J + \lambda I_n]^{-1} J^T \delta \tag{4}$$

where $J = (\partial G(\mu_a))/(\partial\mu_a)$ represents the sensitivity matrix (Jacobian) of dimension NM $\times$ NN with NM representing the number of measurements and NN being the number of nodes. The I_n represents the identity matrix of dimension NN $\times$ NN. The update is represented by $\triangle\mu_a$ and data-model misfit is represented by $\delta = y - G(\mu_a)$. Alternate update equation which is found to be computationally efficient in under-determined cases [42] is given by

$$\triangle\mu_a = J^T[JJ^T + \lambda I_m]^{-1}\delta \tag{5}$$

with I_m representing the identity matrix of dimension NM $\times$ NM. Note that both (4) and (5) form the standard Gauss-Newton minimization method, that gives $\triangle\mu_a$, which is added to current μ_a. The process of finding J, δ, and subsequently $\triangle\mu_a$ is repeated, until the ℓ_2-norm between the δ in subsequent iterations is not improving by more than 2%.

C. Estimation of Optimal Regularization Parameter

A generalized cross-validation (GCV)-based method [43] was used to estimate the optimal regularization parameter in the Tikhonov minimization scheme (standard method). The GCV method is very popular for finding the regularization parameter in cases where the prior information about the noise levels in the experimental data and/or expected image is unavailable [43]. Obtaining an estimate of the regularization parameter λ_{opt} is done by minimizing a function $G(\lambda)$, which is evaluated using the SVD of the Jacobian ($J = USV^T$). The function $G(\lambda)$ is given as [43]

$$G(\lambda) = \frac{\sum_{i=1}^{\text{rank}(J)} \left(\frac{u_i^T \delta}{\sigma_i^2+\lambda^2}\right)^2}{\left(\sum_{i=1}^{\text{rank}(J)} \frac{1}{\sigma_i^2+\lambda^2}\right)^2} \tag{6}$$

where the ith column of the matrix U is represented as u_i and σ_i is the ith singular value of the Jacobian matrix. The estimation of λ_{opt} was achieved through the open-source MATLAB-based regularization toolbox [44]. The estimation of the regularization parameter is performed in the first iteration, and the same value is used for entire image reconstruction procedure.

D. Model-Resolution-Based Convolution/Blur Matrix

The convolution matrix that causes the blur in the reconstructed μ_a is built using the concept of model-resolution. In an ideal noiseless scenario, if the model is perfect, the experimental data matches exactly with the modeled data, i.e., $y = G(\mu_a)$. Now, perform the Taylor expansion of $G(\mu_a)$ around μ_{a0}

$$G(\mu_a) = G(\mu_{a0}) + G'(\mu_a)\tilde{\triangle\mu_a} + (\tilde{\triangle\mu_a})^T G''(\mu_a)\tilde{\triangle\mu_a} + \dots \tag{7}$$

with $G'(\mu_a)$ and $G''(\mu_a)$ representing the Jacobian (J) and the Hessian, respectively, and $\tilde{\triangle\mu_a} = \mu_a - \mu_{a0}$. Linearizing (7) by ignoring the higher order terms results in

$$y = G(\mu_{a0}) + J\tilde{\triangle\mu_a} \tag{8}$$

using $\delta = y - G(\mu_{a0})$ in the above equation results in

$$\delta = J\tilde{\triangle\mu_a} \tag{9}$$

with $\tilde{\triangle\mu_a}$ representing the true update of μ_a in an ideal scenario. Substituting (9) in (4) leads to [34], [45]

$$\triangle\mu_a = \{[J^T J + \lambda I_n]^{-1} J^T J\}\tilde{\triangle\mu_a} = B\tilde{\triangle\mu_a} \tag{10}$$

where $\triangle\mu_a$ is the estimate of the true update $(\tilde{\triangle\mu_a})$ for the optical absorption coefficient μ_a. Ideally for the estimated update $(\triangle\mu_a)$ to be equal to true update $(\tilde{\triangle\mu_a})$, the regularization parameter (λ) should be equal to 0. The ill-posed nature of diffuse optical tomography problem always requires $\lambda > 0$, indicating that $\triangle\mu_a \neq \tilde{\triangle\mu_a}$. The $B = [J^T J + \lambda I_n]^{-1} J^T J$ in (10) is known to be the model-resolution matrix or blurring matrix having a dimension of NN $\times$ NN [34], [45]. The blurring matrix (B) depends on the numerical characteristics of J and the regularization parameter λ, but does not depend on the data. In the ideal noiseless scenario, the B should be an identity matrix (I) with $\triangle\mu_a = \tilde{\triangle\mu_a}$ by having $\lambda = 0$, indicating that there is no blur in the model. For all practical cases, $\lambda > 0$, denoting that at every iteration there is a blur introduced. The aim of this work is to deblur the solution and obtain a close approximation to $\tilde{\triangle\mu_a}$ at every iteration.

Algorithm 1 *Spilt augmented Lagrangian shrinkage algorithm* (SALSA) [46]

AIM: Estimation of $\tilde{\triangle\mu_a}$ in Eq. 10
INPUT: B, $\triangle\mu_a$, λ_{l1}, α, N_{it}.
OUTPUT: $\tilde{\triangle\mu_a}$
Initialize: $d = 0$
1. $\tilde{\triangle\mu_a} = B^T\triangle\mu_a$ and $F = B^T B + \alpha I$
for $k = 1, 2, \cdots N_{it}$
2. v = soft($\tilde{\triangle\mu_a} + d$, $(0.5\lambda_{l1})/\alpha$)-d
3. $\tilde{\triangle\mu_a} = F^{-1}(B^T\triangle\mu_a + \alpha v)$
4. $d = \tilde{\triangle\mu_a} - v$
end

III. Basis Pursuit Deconvolution in Diffuse Optical Tomography

As the update obtained using (4) is blurred by B [(10)], the aim will be here to obtain the true (or close approximate) update $(\tilde{\triangle\mu_a})$ by deconvolution.

A. Basis Pursuit Deconvolution

The deconvolution problem is one of the classical inverse problems, where the aim will be to obtain a deconvolved (unblurred) image from a blurred version of the image. There are several approaches proposed for achieving this [43], with Basis pursuit deconvolution being state of the art [22], [23]. In this approach, the penalty function is based on ℓ_1-norm, which promotes sparseness and sharp features, compared to traditional ℓ_2-norm based penalty [22], [23]. The objective function in this case becomes

$$\tilde{\Omega} = \left\| B\tilde{\triangle\mu_a} - \triangle\mu_a \right\|_2^2 + \lambda_{l1}\|\tilde{\triangle\mu_a}\|_1. \tag{11}$$

This objective function can be minimized using *spilt augmented Lagrangian shrinkage algorithm* (SALSA) [35], [46], [47]. The SALSA algorithm is known to have high convergence speed among all existing ℓ_1-norm based algorithms, enabled via variable splitting of minimization problem [32]. This conversion is achieved using an alternating direction method of multipliers (ADMM), which is based on augmented Lagrangian method

(ALM) [35], [46]. The details of the algorithm is given in [35], [46], it is only briefly reviewed here.

The basic steps needed for SALSA are given in Algorithm 1. The inputs B and $\triangle\mu_a$ are obtained using (10) and (5), respectively. The λ_{l1} is the regularization parameter for this deconvolution problem and typically chosen heuristically. The other reconstruction parameter that is used in this scheme is α, which has similar functionality as λ_{l1} except, it weighs the ℓ_2-norm of the unknown parameter. The other input to this estimation process is number of iterations, $N_{\rm it}$, typically kept at 100. The ADMM parameter (d), which has similar size of $\tilde{\triangle\mu_a}$, is initialized as zero vector. The initial estimate of $\tilde{\triangle\mu_a}$ is obtained using backprojection-type operation (Step 1 of Algorithm 1). Even though the ℓ_1-norm of the $\tilde{\triangle\mu_a}$ [(11)] leads to convex function, the ℓ_1-norm penalty could become null especially when $\tilde{\triangle\mu_a}$ values are close to zero. To overcome this, a soft threshold is used in Step 2, which gives an approximation to the ℓ_1-norm of $\tilde{\triangle\mu_a}$ and is always nonzero. The soft threshold here represents the maximum value (i.e., maximum absolute value among $\tilde{\triangle\mu_a} + d$ and $(0.5\lambda_{l1})/\alpha$). The Step 3 in here is direct translation of *maximum a posteriori* (MAP) estimate, which utilizes the normal equations. The Step 4 updates the ADMM parameter, ideally when converged to solution there is no update in the d [35], [46]. It is important to note that in all our experiments λ_{l1}/α was kept as 0.01, hence making the number of hyper-parameters to choose as only one. Since there is no universally acceptable algorithm for automated estimation of regularization parameter in ℓ_1-norm based scheme, we have chosen this hyper-parameter (λ_{l1}) heuristically.

It can be clearly seen that SALSA algorithm requires $\mathrm{O}(\mathrm{N_{it}} \times \mathrm{NN}^3)$ operations for obtaining the MAP estimate as size of the B is NN $\times$ NN. This computational complexity can be reduced with utilization of SVD of Jacobian matrix (J) and rewriting this Algorithm 1.

B. SVD-Based Basis Pursuit Deconvolution

The SVD of J can be written as

$$J = USV^T \tag{12}$$

where U and V are orthogonal matrices and S is a diagonal matrix containing the singular values of J (arranged in descending order). Substituting (12) in (4) leads to ([21, Appendix A])

$$\triangle\mu_a = V\Sigma U^T\delta \tag{13}$$

where Σ is the diagonal matrix with diagonal entries as $(S)/((S^2+\lambda))$.

Similarly using (12) in (10) (which defines the B) leads to (derived in Appendix A)

$$B = V\Sigma SV^T. \tag{14}$$

Now rewriting Algorithm 1 in terms of SVD of J results in an equivalent computationally efficient algorithm. The image reconstruction algorithm, including finding $\triangle\mu_a$ is summarized in Algorithm 2. Note that Appendix B gives the derivation pertained to conversion of Step 3 of Algorithm 1 into Step 7 of Algorithm 2.

Algorithm 2 Proposed Method based on SVD of Jacobian

INPUT: y, μ_{a0}, λ, λ_{l1}, α, N_{it}
OUTPUT: μ_a
Initialize: m1 = m2 = 0; it = 1;

1. Compute J and $G(\mu_a)$
2. Estimate $\delta_{it} = y - G(\mu_a)$; m2 = $||\delta_{it}||_2{}^2$

if $(\frac{m2-m1}{m2}) * 100 > 2$

3. $[U\ S\ V]$ = svd(J); Make $\Sigma = \frac{S}{(S^2+\lambda)}$
4. $\triangle\mu_a = V\Sigma U^T\delta_{it}$.
5. Initialize: $d = 0$; compute $\tilde{\triangle\mu_a} = V^T\Sigma SV\triangle\mu_a$

`for` $k = 1, 2, \cdots N_{it}$

6. v = soft($\tilde{\triangle\mu_a} + d$, $(0.5\lambda_{l1})/\alpha$) - d.
7. $\tilde{\triangle\mu_a} = V\left(\frac{\Sigma S}{(\Sigma S)^2+\alpha I_n}V^T\triangle\mu_a + \frac{\alpha I_n}{(\Sigma S)^2+\alpha I_n}V^Tv\right)$.
8. $d = \tilde{\triangle\mu_a} - v$.

`end`

9. $\mu_a = \mu_a + \tilde{\triangle\mu_a}$.
10. m1 = m2; it = it +1; go to step-1.

else

stop

end

C. Quantitative Metrics

The proposed algorithm was evaluated quantitatively using a metric namely contrast-to-noise ratio (CNR) defined as [48]

$$\mathrm{CNR} = \frac{\mu_{\rm roi} - \mu_{\rm back}}{(\sigma^2_{\rm roi}a_{\rm roi} + \sigma^2_{\rm back}a_{\rm back})^{\frac{1}{2}}} \tag{15}$$

where $\mu_{\rm roi}$ and $\mu_{\rm back}$ represents the mean value of optical absorption coefficient of the region of interest (ROI) and the background, respectively. The variance of optical absorption coefficient of the ROI and the background is represented as $\sigma^2_{\rm roi}$ and $\sigma^2_{\rm back}$. The ratio of the areas in ROI and background is given as $a_{\rm roi} = (A_{\rm roi})/(A_{\rm tot})$ and $a_{\rm back} = (A_{\rm back})/(A_{\rm tot})$. The higher the CNR better is the image reconstruction and differentiability of tumor and the background [48]. An human eye can perceive the difference between the tumor and background if the CNR value is 4 and above.

The efficacy of the proposed scheme was also evaluated using another metric namely Pearson correlation (PC). The PC is defined as [49]

$$\mathrm{PC}\left(\mu_a^{\rm target}, \mu_a^{\rm recon}\right) = \frac{\mathrm{COV}(\mu_a^{\rm target}, \mu_a^{\rm recon})}{\sigma(\mu_a^{\rm target})\sigma(\mu_a^{\rm recon})} \tag{16}$$

where $\mu_a^{\rm target}$ is the expected absorption coefficient distribution and $\mu_a^{\rm recon}$ represents the reconstructed absorption coefficient distribution. The COV is the covariance and σ indicates the standard deviation. This measure describes how well the reconstruction distribution is correlated with the original target distribution.

IV. Numerical and Gelatin Phantom Experiments

A. Numerical Experiments

To assess the effectiveness of the proposed method in terms of the resolution characteristics of the reconstructed image using

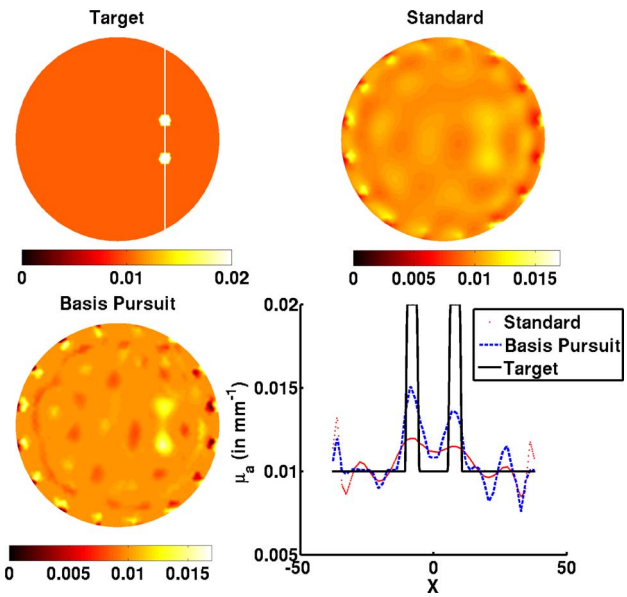

Fig. 1. Comparison of the proposed method with standard Gauss-Newton reconstruction with data containing 1% noise. Top-left image shows the target and the bottom right show the line profile across the line shown in the target image. Reconstruction of the proposed scheme (basis pursuit) and standard method is also shown.

multiple targets, a circular mesh with background optical properties as $\mu_a = 0.01$ mm^{-1}, $\mu_s' = 1$ mm^{-1} and uniform refractive index of 1.33 is considered. The diameter of the circular mesh is 86 mm, it has two circular targets (mimicking tumor region) of 2.5 mm radius separated by a distance of 11 mm centered at (20, 8) and $(20, -8)$ having optical properties as $\mu_a = 0.02$ mm^{-1}, $\mu_s' = 1$ mm^{-1}. The target μ_a distribution is given in the Fig. 1 (top-left corner). Sixteen equidistant fibers were placed on the boundary of the circular domain for data-collection, when one fiber acts as a source rest act as detectors, resulting in collection of $16 \times 15 = 240$ number of measurements (NM). Numerical experimental data was generated on a fine mesh having 10 249 nodes (corresponding to 20 160 linear triangular elements) and the data was added with 1% normally distributed Gaussian noise. The reconstructions were performed on a coarser mesh consisting of 1785 finite element nodes (corresponding to 3418 linear triangular elements) after calibration of the data [50]. Similar to experimental case, the source was modeled as Gaussian source having full width at half maximum of 3 mm [51] and is placed at one mean transport length inside the boundary.

The next numerical experiment that was performed was to test the proposed method robustness to noise in the data. The target here was rectangle in shape [having a length of 25 mm and breadth of 7 mm centered at (0, 15)], mimicking a step function type change in the optical properties. The target distribution is shown in top-left corner of Fig. 2. The data-collection set-up was similar to earlier described case. Here, two noise levels were considered, 1% noisy case (mimicking typical experiment) and 5% case (extreme). In diffuse optical tomographic systems up to 4% noise was reported [52], making 5% noise case as the worst case. The data was generated on a fine mesh consisting

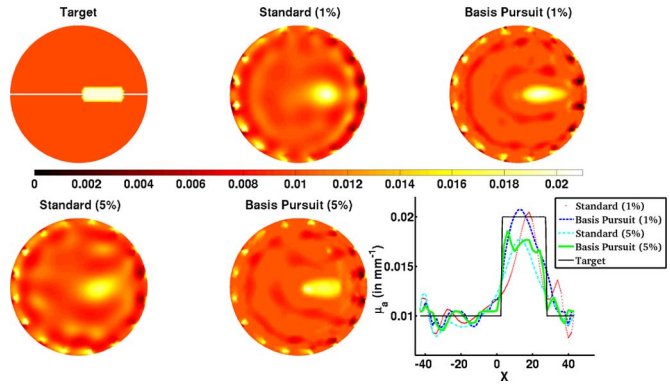

Fig. 2. Similar effort as the previous case with 1% and 5% noisy data, but here the target is rectangular in shape as shown in the top-left corner. Noise level is indicated in the parenthesis.

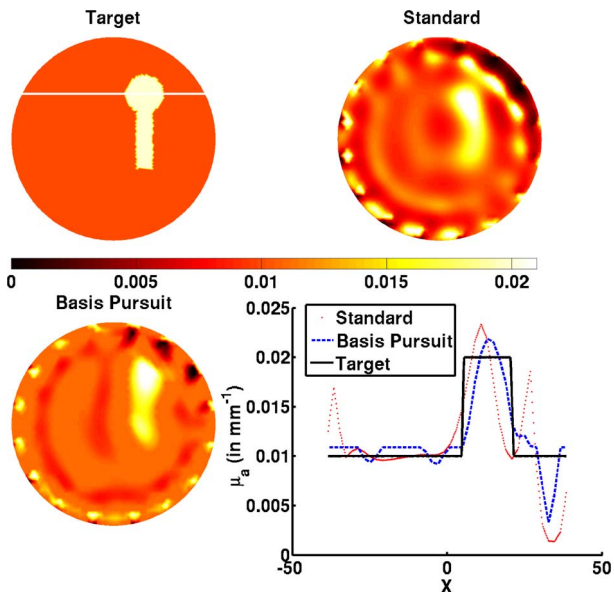

Fig. 3. Similar effort as Fig. 1, with target being irregular in shape.

of 10 249 nodes (corresponding to 20 160 linear triangular elements) The reconstruction was performed on a coarse mesh having 1785 finite element nodes (corresponding to 3418 linear triangular elements).

The targets considered till now were regular in shape, next, a numerical experiment where the target is irregular in shape was considered. The target was in matchstick shape combining rectangle and circle, the rectangle had a length of 25 mm and breadth of 7 mm centered around (13, 0) and circular shape of radius 8 mm was centered at (13, 19), resulting target distribution as shown in the top-left corner of Fig. 3. The data collection geometry and the finite element meshes were same as in the previous case. In here, only the case of 1% noise was considered.

All the above considered cases did not have sharp transitions (edges), hence a numerical experiment was performed by considering a L-shape object, as shown in top-left corner of Fig. 4. The L-shape was generated by combining two rectangles, the horizontal rectangle had a length of 25 mm and breadth of 7 mm centered around $(0, -14)$ and the vertical rectangle had a length of 32 mm and breadth of 7 mm centered around $(-10, 0)$.

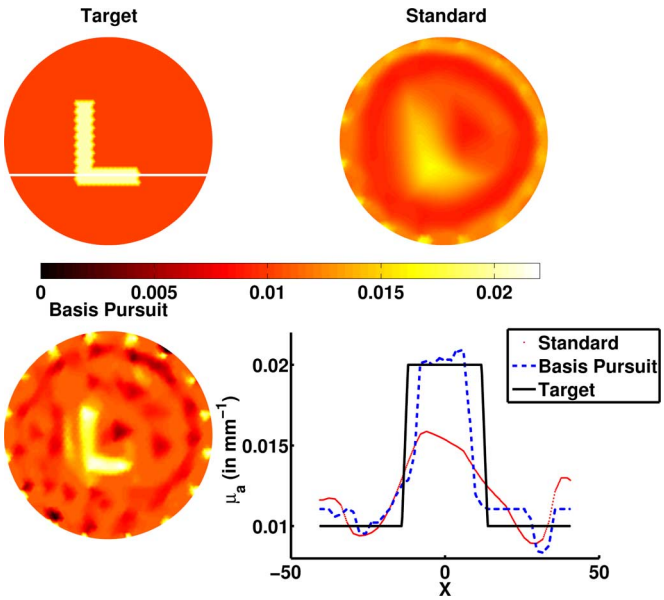

Fig. 4. Similar effort as Fig. 1, with target being in L shape.

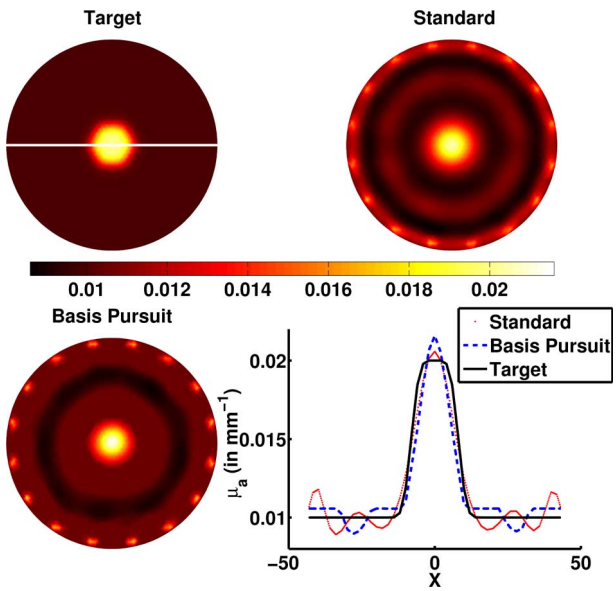

Fig. 5. Similar effort as Fig. 1, with target being circular in shape having a smooth Gaussian variation.

The data was collected in similar fashion to the previously considered cases, and 1% noise was added to the obtained data.

Another numerical experiment was performed to check if the proposed method is able to distinguish between the blur introduced by the regularization parameter and the inherent blur in the experiment. Hence, to simulate this, we considered a circular target with 8 mm radius centered around the origin, further a mean filter was applied on this mesh which resulted in target distribution, as shown in Fig. 5. The same finite element meshes, as in previous case, were used to perform the data collection and reconstruction, and 1% noise was added to the collected data which was used to perform the image reconstruction using the standard and proposed methods.

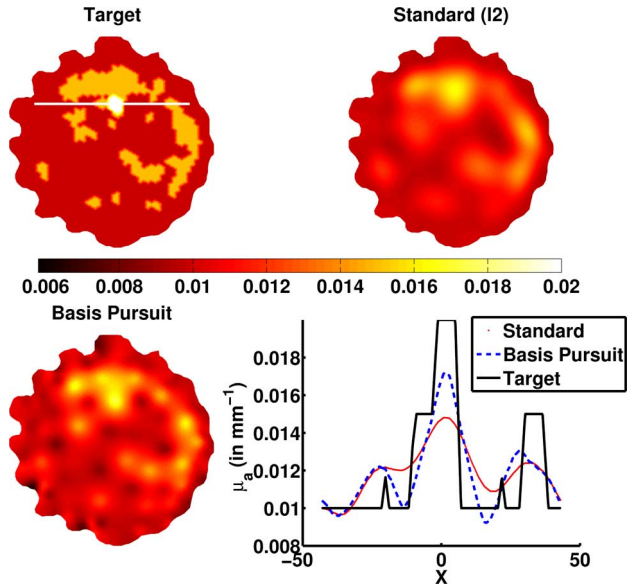

Fig. 6. Comparison of the performance of the standard and the proposed methods in case of a realistic patient (irregular) imaging geometry.

B. Patient Mimicking Numerical Experiment (Irregular Geometry)

To test the efficacy of the proposed method, a patient mimicking irregular geometry is considered having three regions, which are typically observed in the human breast. The irregular geometry was acquired in Dartmouth NIR-MRI set-up [51], here the tissue morphology is obtained using MRI, where both the fatty and fibro-glandular tissue are marked. The optical property of the fibro-glandular region (which is also irregular in nature) was set to $\mu_a = 0.015$ mm^{-1} and $\mu_s' = 1$ mm^{-1}. The other two regions, namely the tumor and fatty tissue have the same optical properties as the previous cases. The target μ_a-distribution is shown in top-left corner of Fig. 6. The experimental data was generated using a fine patient mesh having 5199 nodes (corresponding to 10 208 linear triangular elements). This data was added with 1% normally distributed Gaussian noise. The reconstruction was performed on a coarser mesh consisting of 2002 nodes (corresponding to 3814 linear triangular elements). The data collection strategy was similar to previous cases.

C. Gelatin Phantom Experiment

The proposed basis pursuit deconvolution method performance was also evaluated using a experimental gelatin phantom data [7], that mimics the typical layers observed in Breast imaging. The Gelatin phantom having height 25 mm, radius 43 mm, was made using a mixture of Titanium dioxide (TiO_2) for producing scattering effect and India ink for absorption. Different layers that were observed in a typical breast case were fabricated using hardening heated gelatin solution [having a concentration of 80% of deionized water and 20% of gelatin (G2625, Sigma Inc.)] successively. The optical properties of the outer layer, mimicking the adipose/fat region, was kept at $\mu_a = 0.0065$ mm^{-1} and $\mu_s' = 0.65$ mm^{-1}, having a thickness of 10 mm. The fibro-glandular layer (middle layer) has 76 mm diameter, having the optical properties at $\mu_a = 0.01$ mm^{-1} and $\mu_s' = 1.0$ mm^{-1}. The tumor region is mimicked

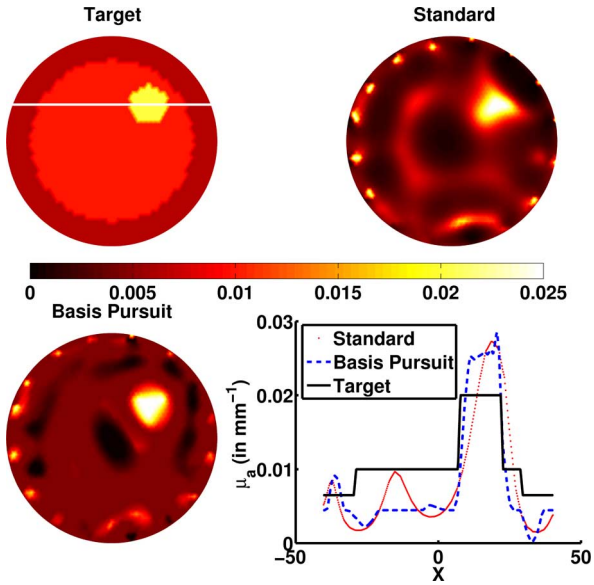

Fig. 7. Evaluation of the performance of the proposed (basis-pursuit deconvolution) method with the standard reconstruction method in case of experimental gelatin phantom. Expected target distribution is given in the top-left corner. The 1-D cross-sectional profile along the dotted line of the target is given in the bottom-right corner.

using a cylindrical hole extending in Z direction filled with intra-lipid mixed with India ink. The optical properties of this tumor region were $\mu_a = 0.02$ mm^{-1} and $\mu_s' = 1.2$ mm^{-1}, having a radius of 8 mm and height of 24 mm. A 2-D cross section of the gelatin phantom was shown in the top-left corner of Fig. 7. The data was collected at 785 nm wavelength. The data collection is done using a single layer of fibers (kept at $z = 0$ mm) leading to 240 data points. The collected data was calibrated using the coarser mesh with 1785 finite element mesh nodes (corresponding to 3418 linear triangular elements) and the reconstruction was performed using this mesh.

All computations were carried out on a Linux workstation with dual six-core Intel Xeon processor of 2.66 GHz speed having 64 GB RAM, with single thread execution. The modeling of light propagation was achieved through MATLAB-based open-source NIRFAST [38], the original SALSA algorithm was based on an open-source package available at [36], and the proposed modification for the SALSA algorithm based on SVD of Jacobian is made available as open-source for enthusiastic users [53].

In all experiments, the reconstruction time for both Algorithm 1 and Algorithm 2 was recorded along with the standard method timings. Moreover, for all reconstruction results the CNR and PC (Section III-C) was computed for quantitative assessment of the reconstructed results.

V. Results

The reconstruction results involving two targets using the standard method (without deconvolution) and proposed method (basis pursuit deconvolution) were shown in Fig. 1. The regularization parameter (λ_{opt}) in the Tikhonov minimization (standard method) was chosen automatically using the GCV method as described in Section II-C. The regularization parameter (λ_{l1}) was chosen heuristically, and the corresponding

TABLE I
Reconstruction Parameters Estimated/Used for the Results Presented in Figs. 1–7 Using Standard Reconstruction and the Proposed (SVD-Based BPD) Method. Note the λ_{opt} Is Same for Both Standard and SVD-Based BPD Methods

Results	Standard (Sec. II.C)	SVD based BPD (Sec. III. B)
Fig. 1	λ_{opt} = 0.0046	λ_{l1} = 0.0001, α = 0.01
Fig. 2 (1% noise)	λ_{opt} = 0.0024	λ_{l1} = 0.015, α = 1.5
Fig. 2 (5% noise)	λ_{opt} = 0.0061	λ_{l1} = 0.015, α = 1.5
Fig. 3	λ_{opt} = 0.0026	λ_{l1} = 0.1, α = 10
Fig. 4	λ_{opt} = 0.0059	λ_{l1} = 0.0001, α = 0.01
Fig. 5	λ_{opt} = 0.0142	λ_{l1} = 0.015, α = 1.5
Fig. 6	λ_{opt} = 0.0048	λ_{l1} = 0.0001, α = 0.01
Fig. 7	λ_{opt} = 0.0034	λ_{l1} = 0.088, α = 8.8

TABLE II
Total Computational Time (in Seconds) Taken for Obtaining the Results Presented in Figs. 1–7 Using Standard, BPD, and SVD-Based BPD. Number of Iterations Taken for Convergence Is Given in the Parenthesis

Result	Standard (Sec. II. B)	BPD (Sec. III. A)	SVD based BPD (Sec. III. B)
Fig. 1	15.58 (25)	36.49 (4)	11.36 (4)
Fig. 2 (1% noise)	17.65 (29)	61.58 (5)	16.12 (5)
Fig. 2 (5% noise)	9.84 (14)	88.94 (7)	21.80 (7)
Fig. 3	16.56 (27)	25.98 (3)	8.57 (3)
Fig. 4	12.62 (18)	35.32 (3)	9.32 (3)
Fig. 5	14.71 (24)	34.71 (4)	10.40 (4)
Fig. 6	14.47 (24)	74.72 (5)	25.01 (5)
Fig. 7	7.94 (11)	110.85 (4)	16.67 (4)

TABLE III
CNR of the Reconstruction Results Presented in Figs. 1–7 Using Standard Reconstruction and the Proposed (SVD-Based BPD) Method

Results	Standard (Sec. II. B)	SVD based BPD (Sec. III. B)
Fig. 1	0.744	2.047
Fig. 2 (1% noise)	0.561	0.858
Fig. 2 (5% noise)	0.571	0.732
Fig. 3	0.297	0.828
Fig. 4	2.05	2.42
Fig. 5	4.806	5.147
Fig. 6	1.161	2.105
Fig. 7	5.026	6.473

value of α was computed to be $\lambda_{l1}/0.01$. The reconstruction parameters for various cases considered here are reported in Table I. The same reconstruction parameters were used in both SVD-based basis pursuit deconvolution (BPD) and the BPD-based image reconstruction. The reconstruction times taken for standard method, traditional basis pursuit method, and SVD-based proposed methods are reported in Table II. The CNR and PC values for the reconstructed images are given in Tables III and IV, respectively. The reconstruction results indicate that the proposed method is able to recover anomalies (tumors) of size 5 mm (typical resolution limit of diffuse optical tomography) more effectively.

The reconstruction results for a horizontal rectangular target absorber for varying noise level are shown in Fig. 2. Table II also lists the total reconstruction time taken for the 1% and 5% noisy data case. The CNR and PC values are reported in the Tables III and IV, respectively. It is evident from the reconstruction results, the standard method fails to recover the shape, whereas

TABLE IV
PEARSON CORRELATION OF THE RECONSTRUCTION RESULTS PRESENTED IN FIGS. 1–7 USING STANDARD RECONSTRUCTION AND THE PROPOSED (SVD-BASED BPD) METHOD

Results	Standard (Sec. II. B)	SVD based BPD (Sec. III. B)
Fig. 1	0.06	0.144
Fig. 2 (1% noise)	0.102	0.156
Fig. 2 (5% noise)	0.104	0.128
Fig. 3	0.071	0.194
Fig. 4	0.143	0.445
Fig. 5	0.715	0.753
Fig. 6	0.734	0.762
Fig. 7	0.130	0.329

the proposed method was able to give close resemblance to the original target shape, even in the high noisy data case (the same could be observed in the PC values, which indicates that the proposed method has close resemblance to the target than the result obtained using standard reconstruction procedure).

The reconstruction results for an irregular absorber (matchstick in shape) using the proposed and standard scheme are shown in Fig. 3. Similar to earlier case, the total computational time, CNR, and the PC values are given in Tables II, III, and IV, respectively. These results indicate that the performance of the proposed method is superior to standard method especially in terms of shape recovery, as seen from the PC values (Table IV).

The reconstruction results corresponding to the L-shaped target is shown in Fig. 4. The reconstruction parameters that were used are reported in Table I. The computational time, CNR, and the PC values are shown in Tables II, III, and IV, respectively. It can be seen from Fig. 4, that the proposed method can efficiently reconstruct sharp changes in the absorption coefficient distribution, hence result in better recovery of shape compared to the standard reconstruction.

Another experiment was performed to check if the proposed method will be able to distinguish between the blur introduced by regularization and the inherent blur in the absorption coefficient distribution. The reconstruction results pertaining to this experiment is shown in Fig. 5. It can be seen that the proposed method is able to retain the inherent blur in the absorption coefficient, and perform the deblurring to remove the blur introduced by the usage of regularization parameter. The same is reflected in the CNR and the PC values reported in Tables III and IV, respectively. The reconstruction parameters and the computational time corresponding to this case are compiled in Tables I and II, respectively.

The reconstruction results corresponding to the patient mimicking case are shown in Fig. 6. It can be seen from the line profile that the proposed method is able to detect the target better than the standard method. The reconstruction parameters, computational time, CNR, and the PC values corresponding to this experiment is shown in Tables I, II, III, and IV, respectively. The CNR value indicates that the proposed method is able to detect the tumor region better than the standard method. Note that for these type of multi-region cases, the CNR is evaluated by considering the fibro-glandular region as the background.

The reconstruction results pertaining to gelatin phantom data were presented in Fig. 7. The total computational time, CNR and the PC values of the reconstruction results are compiled in Tables II, III, and IV, respectively. The results reveal that the shape recovery of the target, especially in these multi-layered target cases, is superior with the proposed method (line-profile plot of Fig. 7).

VI. DISCUSSION

The aim of this work is to introduce a basis pursuit deconvolution approach for improving the diffuse optical tomographic images, where the blur matrix used in deconvolution is built using Jacobian and regularization. The proposed approach requires an additional step of deconvolution compared to the standard approach, making it marginally computationally complex (refer to Table II) compared to the standard approach. The improvement in the reconstruction absorption distribution (refer to Tables III and IV) well justifies the additional computational cost. The computational burden was further reduced with the usage of SVD of Jacobian, which made the total reconstruction procedure to be in the order $\mathrm{O}(\mathrm{NN}^3)$, which is taken for SVD of J. The traditional basis pursuit deconvolution will have a complexity of $\mathrm{O}(\mathrm{N_{it}} * \mathrm{NN}^3)$, making it less desirable in real-time. This image reconstruction can be further accelerated using modern day graphics processing units [54]. It can be noted that computation of the singular value decomposition of the Jacobian is the most expensive step in terms of computation, hence this step can be significantly parallelized using graphics processing units (GPUs) [55], which provide massive parallelization at the desktop level [54].

The two step reconstruction approach is commonly used in diffuse optical imaging [56], [57], primarily to constrain the image space or number of reconstruction parameters. In here, no such constrain is applied, making it first of its kind approach in improving diffuse optical image reconstruction scheme. There were earlier attempts of deconvolving the diffuse optical images [12]–[14], which showed some promise, assumed that the blur kernel was not known. This work introduced a framework to build the blur matrix based on model-resolution and applied state of the art basis pursuit deconvolution to improve the resolution characteristics of reconstructed images (Fig. 1).

It is important to note that the convergence of the proposed scheme is faster when compared to the traditional image reconstruction. This is because a step of image deconvolution is performed at every iteration, producing more accurate solution when compared to traditional scheme (Table II). The shape recovery using the proposed method in all cases presented here was far superior to the reconstructions obtained using traditional method (Figs. 1–7). The cases that were shown here were limited in nature to show the effectiveness of the proposed approach, but the trends observed will be true in general for any case. The proposed method requires heuristic selection of only one hyper-parameter (λ_{l1}) making it more attractive for usage.

There are edge-preserving regularization schemes presented in the literature for diffuse optical tomographic imaging [17]–[20] that can improve the shape recovery of the targets, with a caveat that they all require new parameterization for the parameters. In here, using the standard reconstruction scheme with the aid of resolution characteristics, the proposed scheme was able to recover the shape of the target far superior to standard method.

The ℓ_1-norm based schemes were previously used for performing image reconstruction in diffuse optical tomography [49], and it was shown to be ineffective when the expected optical distribution was not sparse (refer to [49, Fig. 4]). Even in these cases, usage of ℓ_1-norm in the proposed deblurring framework will be able to reconstruct the absorption coefficient well, as we expect the deblurred solution to be an edge enhanced version of the blurred solution, making the usage of ℓ_1-norm minimization, which promotes sparseness and sharp edges, in this framework most optimal. The same was shown in the patient mesh case (Fig. 6).

Even though the concept of model-resolution was introduced well in the earlier works [34], the utilization was limited to building a regularization matrix using this. This work is first of its kind that used the model-resolution matrix as a blur matrix and deconvolved the blur introduced by standard reconstruction algorithms that use ℓ_2-norm in the diffuse optical tomographic image reconstruction process. Moreover, this is also the first attempt to deploy SVD of the Jacobian matrix to reduce the computational complexity in both building the model resolution matrix and performing the deconvolution procedure in diffuse optical tomographic image reconstruction. The computational cost of performing the SVD of the Jacobian matrix is higher especially for 3-D imaging, hence the formulation of model resolution matrix and computation of deconvolved absorption coefficient could be made computationally efficient via deployment of dimensionality reduction techniques, such as least squares QR (LSQR) [48], [58] and Tikhonov-Arnoldi method [59].

The standard method proposed here used only the simplest form of regularization. The advanced regularization schemes have the capability to include more prior information to improve the image characteristics [7], [34], [9]–[11]. In these cases, the model-resolution matrix will also include this information, essentially making the proposed method valid in these cases as well. The work pertaining to this will be taken up in the future to quantify the improvement. The future work will also involve exploring different state of the art deconvolution algorithms.

Even though this work is mostly intended for diffuse optical tomography, the developed methodology could be explored for other imaging techniques whose characteristics are similar to diffuse optical tomography, like electrical impedance tomography [60], bioluminescence tomography, fluorescence optical tomography [61], and electrical capacitance tomography [62].

VII. Conclusion

The diffuse optical tomographic imaging has been a main contender to become adjunct imaging modality for breast and brain imaging. The image reconstruction procedure is highly ill-posed, necessitating the usage of regularization, which makes the reconstructed images loose sharp features. In this work, a basis pursuit deconvolution approach that uses model-resolution matrix was introduced as an additional step in the image reconstruction procedure to improve the reconstructed image characteristics. Moreover, the algorithm was further made computationally efficient using a SVD of the sensitivity (Jacobian) matrix. It was shown that the reconstructed images using the proposed method also display better contrast to noise ratios compared to the results obtained using standard reconstruction method.

Appendix A
Model Resolution Matrix Using SVD of Jacobian

Consider the SVD of the Jacobian (J) resulting in singular value matrix, left and right orthogonal matrices to be S, U, and V, respectively. The model resolution matrix from (10) is defined as

$$B = [J^T J + \lambda I_n]^{-1}(J^T J) \tag{17}$$

with I_n representing the identity matrix of dimension NN $\times$ NN. Substituting (12) into (17) leads to

$$B = [VSU^T USV^T + \lambda I_n]^{-1}(VSU^T USV^T). \tag{18}$$

Since the matrix U is an orthogonal $UU^T = I_m$ giving us

$$B = [VS^2V^T + \lambda I_n]^{-1}(VS^2V^T). \tag{19}$$

Using $VV^T = I_n$, the above equation can be rewritten as

$$B = [VS^2V^T + \lambda VV^T]^{-1}(VS^2V^T). \tag{20}$$

This can be rewritten as

$$B = [V[S^2 + \lambda]V^T]^{-1}(VS^2V^T). \tag{21}$$

Expanding the inverse makes it

$$B = (V^T)^{-1}[S^2 + \lambda]^{-1}V^{-1}(VS^2V^T). \tag{22}$$

Simplifying using $V^T = V^{-1}$ and rearranging terms results in

$$B = V\frac{1}{S^2 + \lambda}V^T VS^2V^T. \tag{23}$$

Using $V^T V = I_n$, in (23) results in

$$B = V\frac{S^2}{S^2 + \lambda}V^T. \tag{24}$$

The singular value matrix of B can be written as $(S^2)/(S^2 + \lambda) = \Sigma S$ (where $\Sigma = (S)/(S^2 + \lambda)$) making

$$B = V\Sigma SV^T \tag{25}$$

Appendix B
Rewriting Step 3 of Algorithm 1 Using SVD of J

The deconvolved update $\tilde{\triangle\mu_a}$ is Step 3 of Algorithm 1 is given by

$$\tilde{\triangle\mu_a} = [B^T B + \alpha I_n]^{-1}(B^T \triangle\mu_a + \alpha v). \tag{26}$$

Substituting the SVD of B given by (25) gives

$$\tilde{\triangle\mu_a} = [V\Sigma SV^T V\Sigma SV^T + \alpha I_n]^{-1}(V\Sigma SV^T \triangle\mu_a + \alpha v) \tag{27}$$

with $\Sigma = (S)/(S^2 + \lambda)$. Substituting $V^T V = I_n$ in (27) gives

$$\tilde{\triangle\mu_a} = [V(\Sigma S)^2 V^T + \alpha V V^T]^{-1}(V\Sigma S V^T \triangle\mu_a + \alpha v). \tag{28}$$

Taking the inverse in the above equation and rearranging the terms results in

$$\tilde{\triangle\mu_a} = \left(V \frac{1}{(\Sigma S)^2 + \alpha I_n} V^T\right)(V\Sigma S V^T \triangle\mu_a + \alpha v). \tag{29}$$

Multiplying the terms in the (29) leads to

$$\tilde{\triangle\mu_a} = V \frac{\Sigma S}{(\Sigma S)^2 + \alpha I_n} V^T \triangle\mu_a + V \frac{\alpha I_n}{(\Sigma S)^2 + \alpha I_n} V^T v. \tag{30}$$

The above equation can be rewritten as

$$\tilde{\triangle\mu_a} = V\left(\frac{\Sigma S}{(\Sigma S)^2 + \alpha I_n} V^T \triangle\mu_a + \frac{\alpha I_n}{(\Sigma S)^2 + \alpha I_n} V^T v\right). \tag{31}$$

ACKNOWLEDGMENT

The authors would like to thank the anonymous reviewers for their invaluable comments that improved this manuscript considerably.

REFERENCES

[1] D. A. Boas, D. H. Brooks, E. L. Miller, C. A. DiMarzio, M. Kilmer, R. J. Gaudette, and Q. Zhang, "Imaging the body with diffuse optical tomography," *IEEE Signal Process. Mag.*, vol. 18, no. 6, pp. 57–75, Nov. 2001.

[2] A. Gibson, J. C. Hebden, and S. R. Arridge, "Recent advances in diffuse optical tomography," *Phys. Med. Biol.*, vol. 50, pp. R1–R43, 2005.

[3] T. Durduran, R. Choe, W. B. Baker, and A. G. Yodh, "Diffuse optics for tissue monitoring and tomography," *Rep. Prog. Phys.*, vol. 73, p. 076701, 2010.

[4] D. R. Leff, O. J. Warren, L. C. Enfield, A. Gibson, T. Athanasiou, D. K. Patten, J. Hebden, G. Z. Yang, and A. Darzi, "Diffuse optical imaging of the healthy and diseased breast: A systematic review," *Breast Cancer Res. Treat.*, vol. 108, pp. 9–22, 2008.

[5] S. R. Arridge and J. C. Schotland, "Optical tomography: Forward and inverse problems," *Inv. Probl.*, vol. 25, p. 123010, 2009.

[6] S. R. Arridge and J. C. Hebden, "Optical imaging in medicine: II. Modelling and reconstruction," *Phys. Med. Biol.*, vol. 42, pp. 841–853, 1997.

[7] P. K. Yalavarthy, B. W. Pogue, H. Dehghani, and K. D. Paulsen, "Weight-matrix structured regularization provides optimal generalized least-squares estimate in diffuse optical tomography," *Med. Phys.*, vol. 34, pp. 2085–2098, 2007.

[8] B. W. Pogue, S. C. Davis, F. Leblond, M. A. Mastanduno, H. Dehghani, and K. D. Paulsen, "Implicit and explicit prior information in near-infrared spectral imaging: Accuracy, quantification and diagnostic value," *Phil. Trans. R. Soc. A*, vol. 369, pp. 4531–4557, 2011.

[9] P. Hiltunen, D. Calvetti, and E. Somersalo, "An adaptive smoothness regularization algorithm for optical tomography," *Opt. Exp.*, vol. 16, pp. 19957–19977, 2008.

[10] C. Panagiotou, S. Somayajula, A. P. Gibson, M. Schweiger, R. M. Leahy, and S. R. Arridge, "Information theoretic regularization in diffuse optical tomography," *J. Opt. Soc. Am. A*, vol. 26, pp. 1277–1290, 2009.

[11] P. Hiltunen, S. Sarkka, I. Nissila, A. Lajunen, and J. Lampinen, "State space regularization in the non-stationary inverse problem for diffuse optical tomography," *Inv. Problems*, vol. 27, p. 025009, 2011.

[12] C. L. Matson, "Deconvolution-based spatial resolution in optical diffusion tomography," *App. Opt.*, vol. 40, pp. 5791–5801, 2001.

[13] S. Jefferies, K. Schulze, C. Matson, K. Stoltenberg, and E. K. Hege, "Blind deconvolution in optical diffusion tomography," *Opt. Exp.*, vol. 10, pp. 46–53, 2002.

[14] Y. Xu, H. L. Graber, Y. Pei, and R. L. Barbour, "Improved accuracy of reconstructed diffuse optical tomographic images by means of spatial deconvolution: Two dimensional quantitative characterization," *App. Opt.*, vol. 44, pp. 2115–2139, 2005.

[15] A. K. Jain and S. Ranganath, "Applications of two dimensional spectral estimations in image restoration," in *Proc. IEEE Int. Conf. Acoust., Speech, Signal Process.*, 1981, pp. 1113–1116.

[16] B. R. Hunt, "The application of constrained least square estimation to image restoration by digital computer," *IEEE Trans. Computers*, vol. 22, pp. 805–812, 1973.

[17] T. Raveendran, S. Gupta, R. M. Vasu, and D. Roy, "A pseudo-time EnKF incorporating shape based reconstruction for diffuse optical tomography," *Med. Phys.*, vol. 39, pp. 1092–1101, 2012.

[18] G. Boverman, E. L. Miller, D. H. Brooks, D. Isaacson, Q. Fang, and D. A. Boas, "Estimation and statistical bounds for three-dimensional polar shapes in diffuse optical tomography," *IEEE Trans. Med. Imag.*, vol. 27, no. 6, pp. 752–765, Jun. 2008.

[19] L. Y. Chen, M. C. Pan, and M. C. Pan, "Implementation of edge-preserving regularization for frequency-domain diffuse optical tomography," *Appl. Opt.*, vol. 51, pp. 43–54, 2012.

[20] L. Y. Chen, M. C. Pan, and M. C. Pan, "Flexible near-infrared diffuse optical tomography with varied weighting functions of edge-preserving regularization," *Appl. Opt.*, vol. 52, pp. 1173–1182, 2013.

[21] S. Gupta, P. K. Yalavarthy, D. Roy, D. Piao, and R. M. Vasu, "Singular value decomposition based computationally efficient algorithm for rapid dynamic near-infrared diffuse optical tomography," *Med. Phys.*, vol. 36, pp. 5559–5567, 2009.

[22] E. Candes and M. Wakin, "An introduction to compressive sampling," *IEEE Signal Process. Mag.*, vol. 25, no. 2, pp. 21–30, Mar. 2008.

[23] J. Romberg, "Imaging via compressive sampling," *IEEE Signal Process. Mag.*, vol. 25, no. 2, pp. 14–20, Mar., 2008.

[24] S. F. Cotter, B. D. Rao, K. Engan, and K. Kreutz-Delgado, "Sparse solutions to linear inverse problems with multiple measurement vectors," *IEEE Trans. Signal Process.*, vol. 53, no. 7, pp. 2477–2488, Jul. 2005.

[25] D. Malioutov, M. Cetin, and A. Willsky, "A sparse signal reconstruction perspective for source localization with sensor arrays," *IEEE Trans. Signal Process.*, vol. 53, no. 8, pp. 3010–3022, Aug. 2005.

[26] D. P. Wipf and B. D. Rao, "An empirical Bayesian strategy for solving the simultaneous sparse approximation problem," *IEEE Trans. Signal Process.*, vol. 55, no. 7, pp. 3704–3716, Jul. 2007.

[27] M. Suzen, A. Giannoula, and T. Durduran, "Compressed sensing in diffuse optical tomography," *Opt. Exp.*, vol. 18, pp. 23676–23690, 2010.

[28] N. Cao, A. Nehorai, and M. Jacobs, "Image reconstruction for diffuse optical tomography using sparsity regularization and expectation-maximization algorithm," *Opt. Exp.*, vol. 15, pp. 13695–13708, 2007.

[29] V. C. Kavuri, Z. J. Lin, F. Tian, and H. Liu, "Sparsity enhanced spatial resolution and depth localization in diffuse optical tomography," *Biomed. Opt. Exp.*, vol. 3, pp. 943–957, 2012.

[30] C. B. Shaw and P. K. Yalavarthy, "Effective contrast recovery in rapid dynamic near-infrared diffuse optical tomography using ℓ_1-norm-based linear image reconstruction method," *J. Biomed. Opt.*, vol. 17, p. 086009, 2012.

[31] O. K. Lee, J. M. Kim, Y. Bresler, and J. C. Ye, "Compressive diffuse optical tomography: Non-iterative exact reconstruction using joint sparsity," *IEEE Trans. Med. Imag.*, vol. 30, no. 5, pp. 1129–1142, May 2011.

[32] O. Lee and J. C. Ye, "Joint sparsity-driven non-iterative simultaneous reconstruction of absorption and scattering in diffuse optical tomography," *Opt. Exp.*, vol. 21, pp. 26589–26604, 2013.

[33] J. A. Fessler and W. L. Rogers, "Spatial resolution properties of penalized-likelihood image reconstruction methods: Space-invariant tomographs," *IEEE Trans. Image Process.*, vol. 5, no. 9, pp. 1346–1358, Sep. 1996.

[34] S. H. Katamreddy and P. K. Yalavarthy, "Model-resolution based regularization improves near infrared diffuse optical tomography," *J. Opt. Soc. Am. Opt. Image Sci. Vis.*, vol. 29, pp. 649–656, 2012.

[35] M. Figueiredo, J. Bioucas-Dias, and M. Afonso, "Fast frame-based image deconvolution using variable splitting and constrained optimization," in *IEEE Workshop on Statistical Signal Processing*, 2009, pp. 109–112.

[36] I. Selesnick, Introduction to sparsity in signal processing [Online]. Available: http://cnx.org/content/m43545/1.3/ 2012

[37] H. Dehghani, S. Srinivasan, B. W. Pogue, and A. Gibson, "Numerical modelling and image reconstruction in diffuse optical tomography," *Phil. Trans. R. Soc. A*, vol. 367, pp. 3073–3093, 2009.

[38] H. Dehghani, M. E. Eames, P. K. Yalavarthy, S. C. Davis, S. Srinivasan, C. M. Carpenter, B. W. Pogue, and K. D. Paulsen, "Near infrared optical tomography using NIRFAST: Algorithms for numerical model and image reconstruction algorithms," *Commun. Numer. Meth. Eng.*, vol. 25, pp. 711–732, 2009.

[39] S. R. Arridge and M. Schweiger, "Photon-measurement density functions. Part 2: Finite-element-method calculations," *Appl. Opt.*, vol. 34, pp. 8026–8037, 1995.

[40] M. Schweiger, S. R. Arridge, M. Hiraoka, and D. T. Delpy, "The finite element model for the propagation of light in scattering media: Boundary and source conditions," *Med. Phys.*, vol. 22, pp. 1779–1792, 1995.

[41] B. W. Pogue and M. S. Patterson, "Review of tissue simulating phantoms for optical spectroscopy, imaging and dosimetry," *J. Biomed. Opt.*, vol. 11, p. 041102, 2006.

[42] P. K. Yalavarthy, D. R. Lynch, B. W. Pogue, H. Dehghani, and K. D. Paulsen, "Implementation of a computationally efficient least-squares algorithm for highly under-determined three-dimensional diffuse optical tomography problems," *Med. Phys.*, vol. 35, pp. 1682–1697, 2008.

[43] P. C. Hansen, J. G. Nagy, and D. P. O. Leary*, Deblurring Images: Matrices, Spectra, and Filtering*, 1st ed. Philadelphia, PA: SIAM, 2006.

[44] P. C. Hansen, "Regularization tools version 4.0 for MATLAB 7.3," *Numer. Algorit.*, vol. 46, pp. 189–194, 2007.

[45] M. S. Zhdanov*, Geophysical Inverse Theory and Regularization Problems*, 1st ed. New York: Elsevier, 2002.

[46] M. V. Afonso, J. M. Bioucas-Dias, and M. A. T. Figueiredo, "Fast image recovery using variable splitting and constrained optimization," *IEEE Trans. Image Process.*, vol. 19, no. 9, pp. 2345–2356, Sep. 2010.

[47] A. Chambolle, "An algorithm for total variation minimization and applications," *J. Math. Imag. Vis.*, vol. 20, pp. 89–97, 2004.

[48] J. Prakash and P. K. Yalavarthy, "A LSQR-type method provides a computationally efficient automated optimal choice of regularization parameter in diffuse optical tomography," *Med. Phys.*, vol. 40, p. 033101, 2013.

[49] J. Prakash, C. B. Shaw, R. Manjappa, R. Kanhirodan, and P. K. Yalavarthy, "Sparse recovery methods hold promise for diffuse optical tomographic image reconstruction," *IEEE J. Sel. Topics Quant. Electron.*, vol. 20, no. 2, p. 6800609, Mar./Apr. 2014.

[50] B. W. Pogue, K. D. Paulsen, C. Abele, and H. Kaufman, "Calibration of near infrared frequency-domain tissue spectroscopy for absolute absorption coefficient quantitation in neonatal head-simulating phantoms," *J. Biomed. Opt.*, vol. 5, pp. 182–193, 2000.

[51] B. Brooksby, S. Jiang, C. Kogel, M. Doyley, H. Dehghani, J. B. Weaver, S. P. Poplack, B. W. Pogue, and K. D. Paulsen, "Magnetic resonance guided near-infrared tomography of the breast," *Rev. Sci. Instrum.*, vol. 75, pp. 5262–5270, 2004.

[52] G. Gulsen, B. Xiong, O. Birgul, and O. Nalcioglu, "Design and implementation of a multifrequency near-infrared diffuse optical tomography system," *J. Biomed. Opt.*, vol. 11, p. 014020, 2006.

[53] Model-resolution based basis pursuit deconvolution improves diffuse optical tomographic imaging [Online]. Available: https://sites.google.com/site/sercmig/home/dotbpd Apr. 25, 2013

[54] J. Prakash, V. Chandrasekharan, V. Upendra, and P. K. Yalavarthy, "Accelerating frequency-domain diffuse optical tomographic image reconstruction using graphics processing units," *J. Biomed. Opt.*, vol. 15, p. 066009, 2010.

[55] S. Lahabar and P. J. Narayanan, "Singular value decomposition on GPU using CUDA," in *Proc. IEEE Int. Symp. Parallel Distrib. Process.*, May 23–29, 2009, pp. 1–10.

[56] S. Srinivasan, B. W. Pogue, H. Dehghani, S. Jiang, X. Song, and K. D. Paulsen, "Improved quantification of small objects in near-infrared diffuse optical tomography," *J. Biomed. Opt.*, vol. 9, pp. 1161–1171, 2004.

[57] B. Kanmani and R. M. Vasu, "Diffuse optical tomography through solving a system of quadratic equations: Theory and simulations," *Phys. Med. Biol.*, vol. 51, pp. 981–998, 2006.

[58] J. Prakash, A. S. Raju, C. B. Shaw, M. Pramanik, and P. K. Yalavarthy, "Quantitative photoacoustic tomography with model-resolution based basis pursuit deconvolution," *Biomed. Opt. Exp.*, 2014, submitted for publication.

[59] P. Novati and M. R. Russo, "A GCV based Arnoldi-Tikhonov regularization method," BIT Numer. Math. 2013.

[60] L. Borcea, "Electrical impedance tomography," *Inv. Probl.*, vol. 18, pp. R99–R136, 2002.

[61] C. Darne, Y. Lu, and E. M. Sevick-Muraca, "Small animal fluorescence and bioluminescence tomography: A review of approaches, algorithms and technology update," *Phys. Med. Biol.*, vol. 59, pp. R1–R64, 2014.

[62] M. Soleimani, P. K. Yalavarthy, and H. Dehghani, "Helmholtz type regularization method for permittivity reconstruction using experimental phantom data of electrical capacitance tomography," *IEEE Trans. Instrum. Meas.*, vol. 59, no. 1, pp. 78–83, Jan. 2010.